Ocean Modelling 97 (2016) 16–26

Contents lists available at ScienceDirect

Ocean Modelling

journal homepage: www.elsevier.com/locate/ocemod

On improving the accuracy of the M_2 barotropic tides embedded in a high-resolution global ocean circulation model

Hans E. Ngodock[a,*], Innocent Souopgui[b], Alan J. Wallcraft[a], James G. Richman[a], Jay F. Shriver[a], Brian K. Arbic[c]

[a] Oceanography Division, Naval Research Laboratory, Code 7320, Stennis Space Center, MS, USA
[b] Department of Marine Sciences, University of Southern Mississippi, Stennis Space Center, MS, USA
[c] Department of Earth and Environmental Sciences, University of Michigan, Ann Arbor, MI, USA

ARTICLE INFO

Article history:
Received 1 June 2015
Revised 1 October 2015
Accepted 11 October 2015
Available online 3 November 2015

Keywords:
Barotropic tides
HYcom
State augmentation
Ensemble Kalman filter
Data assimilation
Forcing correction

ABSTRACT

The ocean tidal velocity and elevation can be estimated concurrently with the ocean circulation by adding the astronomical tidal forcing, parameterized topographic internal wave drag, and self-attraction and loading to the general circulation physics. However, the accuracy of these tidal estimates does not yet match accuracies in the best data-assimilative barotropic tidal models. This paper investigates the application of an augmented state ensemble Kalman Filter (ASEnKF) to improve the accuracy of M_2 barotropic tides embedded in a 1/12.5° three-dimensional ocean general circulation model. The ASEnKF is an alternative to the techniques typically used with linearized tide-only models; such techniques cannot be applied to the embedded tides in a non-linear eddying circulation. An extra term, meant to correct for errors in the tide model due to imperfectly known topography and damping terms, is introduced into the tidal forcing. Ensembles of the model are created with stochastically generated forcing correction terms. The discrepancies for each ensemble member with TPXO, an existing data-assimilative tide model, are computed. The ASEnKF method yields an optimal estimate of the model forcing correction terms, that minimizes resultant root mean square (RMS) tidal sea surface elevation error with respect to TPXO, as well as an estimate of the tidal elevation. The deep-water, global area-averaged RMS sea surface elevation error of the principal lunar semidiurnal tide M_2 is reduced from 4.4 cm in a best-case non-assimilative solution to 2.6 cm. The largest elevation errors in both the non-assimilative and ASEnKF solutions are in the North Atlantic, a highly resonant basin. Possible pathways for achieving further reductions in the RMS error are discussed.

Published by Elsevier Ltd.

1. Introduction

The tides can be estimated concurrently with the ocean circulation by adding the astronomical tidal forcing, parameterized topographic internal wave drag, and self-attraction and loading to the general circulation physics (Arbic et al., 2010). However, the accuracy of the tidal elevations in these ocean simulations with embedded tides does not yet match accuracies in the best data-assimilative barotropic tidal models (Stammer et al., 2014). In this paper we demonstrate that an augmented state ensemble Kalman Filter (ASEnKF) can be used to reduce the sea surface elevation errors of barotropic tides embedded in a high-resolution three-dimensional ocean circulation model. The model utilized here is the 1/12.5° horizontal resolution HYbrid Coordinate Ocean Model (HYCOM; Chassignet et al., 2009), which is the current global operational model run by the United States Navy (Metzger et al., 2014). In the near future the Navy plans to run an operational model based on global 1/25° HYCOM with embedded tides. Because the model is operational, the accuracy of the tides is extremely important. However, current methods used in data-assimilative hydrodynamic barotropic tide-only models (e.g., the TPXO model of Egbert and Erofeeva, 2002, the FES model of Lyard et al., 2006, and the HAMTIDE model of Taguchi et al., 2014) are carried out in the frequency domain, take advantage of the absence of non-tidal signals, and assume linearized equations of motion. Hence these techniques cannot be used in a model where the tides are embedded within a fully nonlinear ocean general circulation model. We are therefore motivated to improve the accuracy of the tides in HYCOM using a method that does not require the model equations to be linearized and which can be applied to a model in the time domain rather than frequency domain, i.e. the ASEnKF. The ASEnKF is a new introduction into our HYCOM simulations with concurrent tidal and atmospheric forcing, which up until now have been run with no assimilation applied to either the tides or atmospherically-forced

* Corresponding author. Tel.: +1 228 688 5455.
E-mail address: Hans.Ngodock@nrlssc.navy.mil (H.E. Ngodock).

http://dx.doi.org/10.1016/j.ocemod.2015.10.011
1463-5003/Published by Elsevier Ltd.

motions (Arbic et al., 2010, 2012; Richman et al., 2012; Timko et al., 2012, 2013; Shriver et al., 2012, 2014; Stammer et al., 2014; Müller et al., 2015; Ansong et al., 2015). This paper discusses the ASEnKF method, as well as improvements we plan to make to our application of the ASEnKF in order to further reduce the tidal errors in future studies.

The addition of astronomical tidal forcing to our HYCOM general circulation simulations yields a robust internal tide field (Shriver et al., 2012). Indeed, the simulation of reasonably accurate internal tides requires solving for barotropic tides within a general circulation ocean model. This is because the baroclinic tides are generated from barotropic tidal flow over bathymetry in an ocean with space- and time-varying stratification. The internal tides propagate through a variable ocean where they are scattered and dissipated by the interaction with changing stratification, bottom topography and variable ocean currents. About 25–30% of the global tidal energy dissipation occurs through the nonlinear interactions of internal tides generated over mid-ocean rough topography (Egbert and Ray, 2001; Garrett, 2003). Internal tides are a significant component of the spectrum of internal gravity waves (Garrett and Munk, 1975), and the breaking of internal gravity waves including internal tides drives much of the mixing occurring in the subsurface ocean (Munk and Wunsch, 1998). The resulting mixing affects the large-scale oceanic stratification and circulation (Munk and Wunsch, 1998).

Aside from impacts on the internal gravity wave spectrum and mixing, another motivation for including internal tides in a three-dimensional circulation model is the impact internal tides have on boundary conditions for higher resolution regional models. The operational global three-dimensional HYCOM forecasts provide boundary conditions for such regional models. Because the current configuration of operational global HYCOM does not include tides, a regional model using HYCOM as a boundary forcing must take the tidal forcing from barotropic data-assimilative tide models such as TPXO. Specification of barotropic tides at the boundaries is used even in high-resolution regional models that focus exclusively on internal tides (e.g., Holloway, 1996; Merrifield et al., 2001). However, because TPXO is a barotropic tide model, TPXO boundary conditions preclude the propagation of remotely generated internal tides into regional models. The HYCOM simulations with embedded tides can provide three-dimensional tidal elevations and currents at the boundaries of regional models. Indeed HYCOM is currently one of a small number of models that could be used for this purpose. A recent review of tide models by Stammer et al. (2014) lists only two global general circulation ocean models with tidal forcing: HYCOM and the German consortium project STORMTIDE (Müller et al., 2012), although the pursuit of such models amongst other groups is growing (Waterhouse et al., 2014). Studies have shown that when both barotropic and baroclinic tides are prescribed at the boundary of regional models, significant differences in the tides over the shelf and the energy fluxes of away from the shelf compared to barotropic boundary forcing occur (Kelly and Nash, 2010; Kerry et al., 2013; Ponte and Cornuelle, 2013). Therefore the inclusion of internal tides in boundary forcing of regional models is a necessary step to be taken in the near future.

The accuracy of the internal tides in a model is linked directly to the accuracy of the modeled barotropic tides. A major motivation for our research on the ASEnKF is that improvements in the accuracy of simulated barotropic tides are expected to yield improved internal tides. In Shriver et al. (2012) we showed that internal tide amplitudes in earlier non-assimilative HYCOM solutions, when spatially averaged over known "hotspot" generation regions, are within about 20% of amplitudes averaged over along-track satellite altimeter data (Ray and Mitchum, 1996; Ray and Bryne, 2010) in the same regions. Although the spatial averages are close as noted, the individual peaks and troughs in the HYCOM simulations often do not line up well with peaks and troughs in the along-track altimeter data (Shriver et al., 2012). An eventual goal of the application of the ASEnKF to our HYCOM tides simulations is to improve the accuracy of the internal tides. For the sake of brevity, however, the present paper focuses only on the accuracy of barotropic tides in global HYCOM. The impact of the ASEnKF on the internal tides in HYCOM will be addressed in a future paper.

The barotropic tide errors in our HYCOM simulations (Shriver et al., 2012) may be attributed to several factors: (1) model resolution, especially near the coast; (2) inaccurate bathymetry; (3) inaccurate quadratic bottom friction coefficients; (4) inaccurate estimation of internal tide energy loss near rough bathymetry by the linear topographic internal wave drag parameterization (Arbic et al., 2010) and (5) improper representation of the self-attraction and loading term (Hendershott, 1972). Conceptually these issues can be addressed individually, although this can be a daunting task in the present context. For example, to address the issue of resolution, Lyard et al. (2006) use an unstructured grid within a single layer barotropic model to achieve very fine resolution near the coast and an accurate barotropic tidal solution. This method of increasing model resolution near the coast is currently impossible in HYCOM, which uses a structured grid. Lyard and collaborators have taken advantage of the much lower computational cost of their model to optimize maps of linearized spatially varying quadratic bottom friction, as well as maps of parameterized topographic internal-wave drag and coastal bathymetry, to achieve low barotropic tidal errors (Florent Lyard, personal communication, 2014). Iteratively perturbing the quadratic bottom friction, topographic internal wave drag and bathymetry to achieve optimal tides can be done in single layer tide-only models, but the process becomes computationally prohibitive for a nonlinear three-dimensional circulation model such as HYCOM. In addition, the impact of these perturbations on the non-tidal solution might not be negligible.

For the sake of convenience, we assume the cumulative effects of the error sources mentioned above can be represented by a single barotropic forcing correction term. The question then becomes whether such a correction can be estimated with the help of observations to minimize the error of the modeled barotropic tides with respect to observations. This study provides a positive answer to that question. Understandably, the interpretation of the estimated correction may be complicated due to the potential contribution from many model error sources to the correction. An attempt to sort out those contributions is beyond the scope of this study.

The estimation of the model error and model forcing corrections is an inverse problem that has received some attention in the literature, especially with weak constraint four-dimensional variational (4dvar) data assimilation methods (Bennett, 2002; Ngodock and Carrier, 2014). These methods require the implementation of the tangent linear approximation and adjoint of the dynamical model in consideration. Such development is not feasible with HYCOM because of the highly nonlinear nature of the model, where even the vertical coordinate can change with time. The matter is further complicated by the turbulence closures and the flux-correction transport for the momentum advection scheme in HYCOM.

Another method for estimating the model error and forcing correction in data assimilation is the state augmentation technique from Jazwinski (1970) and Gelb (1974). This method has been applied through the ensemble Kalman filter (EnKF) of Evensen (1994) to hydrology by Reichle et al. (2002), to the Korteweg–de-Vries Burgers model by Zupanski and Zupanski (2006), to the problem of model bias estimation by Baek et al. (2006), and to the observation bias correction problem by Fertig et al. (2009). The state augmentation approach is adopted as the method for estimating the barotropic tide model error and forcing correction in HYCOM mainly for the convenience it offers in the implementation, as detailed below.

This paper goes beyond the classic problem of assimilating tide observations into a hydrodynamic barotropic tide model, i.e. the correction of the tide solution, which has received much attention in the literature (e.g., Egbert et al., 1994; Egbert and Erofeeva, 2002;

Lyard et al., 2006; Taguchi et al., 2014; Stammer et al., 2014; and references therein). Having the correct amplitude and phase of the barotropic component of the tidal constituents is not helpful in the context of a three-dimensional hydrodynamic model, since those amplitudes and phases cannot be included in the multi-layer time-stepped model to generate the desired three-dimensional tidal solution. The correct dynamics are needed in a three-dimensional model to generate both the barotropic and the baroclinic tides. Our intention, therefore, is to use the data assimilation process, specifically the ASEnKF, as a mechanism to estimate the tide model error as well as a correction term engineered to minimize the tide error. In essence, we know that we have an imperfect model, and we use the data assimilation process to correct the model so that tides are predicted accurately. To our knowledge, an approach such as this has not previously been addressed in the tidal modeling literature. We will use the highly accurate satellite-altimetry constrained TPXO tide model as "data" or "observations" of the barotropic tide. In the end, we will not only evaluate the estimated tidal solution (analysis) against the TPXO data that were assimilated, but we will also include optimized model correction terms to generate a new predicted solution in a three-dimensional (3D) ocean circulation model to be compared with available observations, including deep water tide gauges that are independent of the altimetry-constrained TPXO model we use in the ASEnKF.

This paper is organized as follows. The barotropic tidal errors in our prior hydrodynamic model are briefly discussed in Section 2. The state augmentation method and its implementation are discussed in Section 3. Section 4 deals with the application of the ASEnKF for tidal correction and model error estimation. A discussion of the limitations of the current implementation of the ASEnKF and the differences between the estimated tide from the ASEnKF and the predicted tide in the 3D ocean circulation model forced by the ASEnKF forcing correction are given in Section 5. Concluding remarks are presented in Section 6.

2. The prior simulation of barotropic tides in HYCOM

This section describes the prior simulations of the tides in the global model before the application of the ASEnKF. The most accurate global barotropic tides are obtained by data-assimilative hydrodynamic barotropic models with M_2 root mean square (RMS) elevation errors in deep water as small as 0.5 cm (Stammer et al., 2014). The HYCOM tide simulations are forced by both the atmospheric fluxes from the Navy operational global atmospheric prediction systems (NOGAPS, Rosmond et al., 2002; NAVGEM, Hogan et al., 2014), and the astronomical tidal potential. The global HYCOM tidal simulation uses parameterized internal topographic wave drag to account for the breaking of unresolved high vertical mode internal waves (Arbic et al., 2010). As shown by many authors including Arbic et al. (2004), the wave drag impacts the amplitude of tides in models.

For a given surface elevation, the self-attraction and loading (SAL) due to the tidal load deformation of the solid earth, together with the self-gravitation of the tidally deformed ocean and solid earth, can be computed (Henderson, 1972; Ray, 1998). As shown by Gordeev et al. (1977), the SAL impacts the tidal phases significantly, and therefore must be included in ocean models. However, in a tidal model, the surface elevation is not known prior to the estimation of the SAL forcing. A self-consistent way to compute the correct SAL for a tidal model is iterative, starting with an approximate SAL and computing the corresponding surface elevation. The latter surface elevation is used to compute its associated SAL to be applied in the computation of yet another elevation field. This process is iterated until formal convergence, which typically involves only a few iterations for tide-only models. The tidal SAL computation can be iterated because tides are periodic, which allows the SAL to be written in terms of an amplitude and phase that are meaningful from one iteration to the next. One could in principle compute the SAL from the model mass field at every time step, a procedure that would not involve iterations and that would incorporate the SAL effects of non-periodic motions. However, solving for the SAL at every time step is extremely expensive for a hydrodynamic time-stepped model, as discussed by Stepanov and Hughes (2004). The earliest HYCOM tide simulations, described by Arbic et al. (2010) and Shriver et al. (2012), employ a simplified scalar approximation of the SAL (Accad and Pekeris, 1978). The scalar approximation for SAL represents yet another source of error for the tidal solution, in addition to the ones mentioned above.

Shriver et al. (2012) compared 8 barotropic semi-diurnal and diurnal tidal constituents, M_2, S_2, N_2, K_2, K_1, O_1, P_1, and Q_1, obtained from an early long HYCOM simulation, with TPXO 7.2; we designate this initial simulation as **T0** in this paper. Shriver et al. (2012) found significant error levels both in the amplitudes and phases of the tides. For example, the root mean square (RMS) amplitude and amplitude-weighted phase errors for M_2 were 5.56 cm and 5.00 cm, respectively, for a total error of 7.47 cm compared to the 26.6 cm RMS deep water amplitude of M_2 in TPXO 7.2 (Fig. 4 in Shriver et al., 2012). The error in the Shriver et al. (2012) simulation is comparable to the errors in other non-assimilative shallow water tide models, ~7 cm (Jayne and St. Laurent, 2001; Arbic et al., 2004) and ~5 cm (Egbert et al. 2004), but is much larger than the ~0.5 cm errors for the data assimilative tide models (Stammer et al., 2014). The simulations of Jayne and St. Laurent (2001), Arbic et al. (2004) and Egbert et al. (2004) used a rigorous, iterated SAL forcing in contrast to the scalar approximation in this HYCOM simulation. In addition, Egbert et al. (2004) noted that 5–10% random errors in the bathymetry lead to ~8 cm RMS differences in the M_2 amplitude. Errors in the HYCOM simulation are not uniformly distributed over the ocean. As can be seen in the RMS error map in Fig. 1, the largest errors in the M_2 tide occur in the Southern Ocean around Antarctica, in the Atlantic Ocean, around South Africa and the western South Pacific.

Some intermediate developments have been implemented since our early HYCOM simulations described in Shriver et al. (2012) and Stammer et al. (2014). To improve the Southern Ocean tides, the model bathymetry was changed to include the ocean under the floating Antarctic ice shelves. The coarse resolution topographic internal wave drag based upon the Garner (2005) scheme and used by Arbic et al. (2004, 2010) was replaced by a higher resolution Jayne and St. Laurent (2001) (JSL) wave drag scheme. The JSL wave drag was tuned to minimize the RMS sea level elevation error between a barotropic HYCOM M_2 simulation and TPXO8 (Buijsman et al., 2015). The approximate scalar SAL was replaced by an iterated SAL (Buijsman et al., 2015). These changes result in marked improvements in the barotropic tides in a 41 layer global ocean simulation, designated as **T1** in this paper. The global deep-water M_2 error compared to TPXO8 decreases from ~8 cm in the initial simulation **T0** to ~4 cm in this intermediate simulation **T1**. While the tidal elevation error is reduced significantly, the ~4 cm error level is much greater than ~0.5 cm error of the data assimilative tide models discussed in Stammer et al. (2014). Visual inspection of the RMS errors of the initial and intermediate simulations in Fig. 1 shows reduced errors in **T1** for much of the ocean, particularly the Southern Ocean and western Pacific Ocean. However, large errors are found in the Atlantic for both simulations. Note that in **T1**, in order to avoid problems in resolving nearby tidal constituents and the consequent need for long model runs, we have reduced the tidal potential forcing to the 5 leading constituents, M_2, S_2, N_2, K_1 and O_1, which can be distinguished from each other with an analysis based on just 28 days of model output.

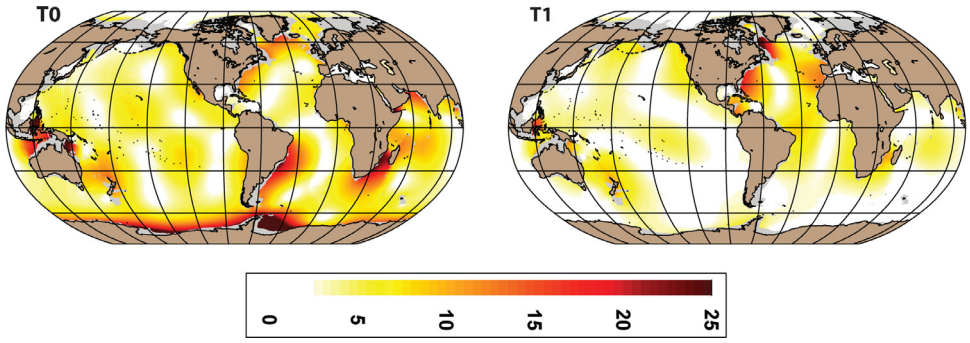

Fig. 1. Maps of the M_2 RMS error (cm) between HYCOM simulations and TPXO8: **T0**, initial 8 constituent simulation with scalar SAL and Garner (2005) wave drag, and **T1**, intermediate 5 constituent simulation with bathymetry extended to include floating Antarctic ice shelves, tuned JSL wave drag and iterated SAL.

3. State augmentation through the ensemble Kalman filter

As noted above, the data assimilative barotropic tide models have much smaller elevation errors than our intermediate solution, **T1**. Potentially, the errors in the HYCOM barotropic tides could be corrected using data assimilation in a state estimation problem. However, knowing the best tidal elevation through state estimation does not help us with predicting the tides in the embedded 3D global model. Our goal is obtaining a tidal solution that minimizes the error compared to observations, and a correction to our dynamical model that will generate accurate tidal elevations and velocities within the running 3D global ocean circulation model. It is admittedly a difficult task to address the error sources individually within a multi-layer high resolution global hydrodynamic model. However, if all the error sources can be combined into one model correction term for the tides, then the problem becomes one of estimating this correction term. We can use an augmented state ensemble Kalman filter algorithm, described below, to obtain an estimate of the minimal error tidal elevation and the model correction needed to generate this elevation.

3.1. State estimation with ensemble Kalman filter

First we will present the framework of an ensemble Kalman filter for state estimation before discussing the state augmentation in the next section. Consider an ocean model that can be written in the form

$$\frac{\partial X}{\partial t} = F(X) + f, \tag{1}$$

where X is the state of the ocean at any given time, F includes the dynamics and physics of the ocean as well as the atmospheric forcing, and f is a generic model error term that could represent unresolved processes, incorrect parameterizations, incorrect bathymetry, or errors in the external atmospheric forcing. The model error f is assumed here to be a random variable that has zero mean with a covariance C_f. Given a vector Y_k of observations at a specific time k during the model integration with the associated vector of observation errors ε_k (with covariance C_k^ε), we can relate the observations to the model state by

$$Y_k = H_k X_k + \varepsilon_k, \tag{2}$$

where H_k is the observation operator associated with the kth observation time. Then, the generalized state estimation problem consists of finding the solution X_k^a, also called the analysis, where the discrepancy between the solution and the observations is minimized in a least squares sense. The analysis is given by

$$X_k^a = X_k + B_k H_k^{\mathrm{T}} \left(H_k B_k H_k^{\mathrm{T}} + C_k^\varepsilon\right)^{-1} (Y_k - H_k X_k), \tag{3}$$

where B_k is the background error covariance and the superscript T denotes the transpose operator. The background error covariance B_k can be prescribed in a functional or operator form (Weaver and Courtier, 2001) or can be modeled with an ensemble (e.g. Evensen, 1994). The analysis is the best estimate of the model state given the observations, background error covariance and observation error covariance. However, our focus is not finding a one-time best estimate of the model state, but obtaining the best correction to the model forcing f to be used with the time varying model dynamics. The latter has not received much attention in the literature compared to the former. In other words, we are not aiming at correcting the model state through data assimilation; rather we want to improve the model with a forcing correction. With this forcing correction, the model solution will be improved for future simulations without further assimilation.

The ensemble approach generates a background error covariance from an ensemble of model solutions X_k^n, $n = 1, 2 \ldots N$ of the form

$$B_k = \frac{1}{N-1} \sum_{n=1}^{N} \left(X_k^n - \overline{X_k}\right)\left(X_k^n - \overline{X_k}\right)^{\mathrm{T}}. \tag{4}$$

In (4) $\overline{X_k}$ denotes the ensemble average or mean and the ensemble of model solutions is obtained by integrating the model (1) with different perturbations added to either the initial condition or the forcing or both.

3.2. Augmented state Kalman filter

The state estimation process can be modified to infer a model forcing correction through the state augmentation technique in which the definition of the state vector is extended to include the correction. The new state vector becomes

$$Z = \begin{pmatrix} X \\ f \end{pmatrix} \tag{5}$$

and the augmented dynamical model (1) becomes

$$\frac{\partial}{\partial t}\begin{pmatrix} X \\ f \end{pmatrix} = \begin{pmatrix} F(X) + f \\ -\rho f \end{pmatrix} + \begin{pmatrix} 0 \\ u \end{pmatrix}, \tag{6}$$

where u is a noise perturbation, designed to yield the correction f, which is modeled as a first-order Markov process with a time decorrelation ρ^{-1}. When the ensemble is generated for the augmented state (5) using (6), the augmented background error covariance calculated by (4) will automatically contain the cross-covariance between the model state X and the forcing correction f. Hence, in the augmented analysis with Z replacing X in (3), an optimal estimate of the forcing correction f is obtained as well as an estimate of the model state X. Apart from an ensemble approach this cross-covariance would otherwise have to be prescribed, which can be a rather difficult task. In all cases discussed below, the ensemble mean of the augmented state Z^a from (3), with Z replacing X, will be referred to as the analysis.

In practice, we can express the model dynamics including the tide as

$$\frac{\partial X}{\partial t} = F(X, \langle T_{\text{pot}}\rangle + \langle \text{SAL}\rangle + \langle \zeta \rangle), \tag{7}$$

where X represents the ocean state comprising the tides, the two-dimensional sea surface height (SSH) and the three-dimensional state of temperature, salinity, zonal and meridional velocities. The operator F includes not only the usual dynamical terms such as advection, pressure gradient, Coriolis, horizontal and vertical mixing, and atmospheric forcing, but also includes forcing from the sum of the tidal potential T_{pot} and the self-attraction and loading SAL, in the hydrodynamic model's pressure equation. The tidal forcing terms are written in angled brackets in (7) because they are defined in frequency space, e.g. as amplitude and phase, or equivalently as real and imaginary components, and the brackets represent the expansion in time for inclusion in the time-stepped hydrodynamic model. In our approach, the tidal forcing or constituents is always expressed as real and imaginary components because this avoids issues with the periodicity of phase. In addition, the generic model error in (1) is now restricted to a tidal model correction ζ, also defined in frequency space, and of the same form as T_{pot} and SAL. This correction represents the aggregated contributions of all the potential tidal error sources mentioned above. In the present context dynamical and forcing errors in the hydrodynamic model are omitted, not because they are necessarily negligible, but because the focus of this study is on the ability to correct tidal errors within the three-dimensional ocean model. Note that with the inclusion of the tidal forcing, the SSH component of the 3D model state X in (7) is the sum of the non-tidal and tidal contributions, SSH_{NT} and $\langle \text{SSH}_{\text{T}}\rangle$ respectively. For the sake of convenience the state variable X is written in the form

$$X = \begin{pmatrix} \text{SSH} \\ X' \end{pmatrix} = \begin{pmatrix} \text{SSH}_{\text{NT}} + \langle \text{SSH}_{\text{T}}\rangle \\ X' \end{pmatrix} \tag{8}$$

where X' denotes all the model variables mentioned above with the exception of SSH. Solving (7) over time yields a time series of X denoted $X_{\text{TR}} = (X_1, X_2, \ldots X_N)$, from which a SSH time series denoted SSH_{TR} is extracted. A harmonic analysis of SSH_{TR} yields SSH_{T} in the frequency space. Thus, SSH_{T} is obtained through a succession of operations that can be written as

$$\text{SSH}_{\text{T}} = H_A \bullet P_{\text{SSH}} \bullet \Psi(X, \langle T_{\text{pot}}\rangle + \langle \text{SAL}\rangle + \langle \zeta \rangle) \tag{9}$$

where H_A denotes the harmonic analysis operator, P_{SSH} is the extraction of SSH from the model solution, and $\Psi(X, \langle T_{\text{pot}}\rangle + \langle \text{SAL}\rangle + \langle \zeta \rangle) = X_{\text{TR}}$, the model solution time series obtained from solving (7).

The augmented state ensemble consists of the barotropic tidal elevation for each member and the associated tidal forcing perturbation, both in frequency space, i.e.

$$Z = \begin{pmatrix} \text{SSH}_{\text{T}} \\ \zeta \end{pmatrix}. \tag{10}$$

The ASEnKF is applied to this ensemble with the assumption that the correlation between $\langle \text{SSH}_{\text{T}}\rangle$ and the remaining model variables of the hydrodynamic model is zero. The background error covariance is estimated for the augmented state Z in (10) from the ensemble using (4).

3.3. Ensemble generation

The tidal forcing perturbations are generated in the frequency space and expanded in the space-time domain to be embedded in the time-stepping three-dimensional model (HYCOM). A 100-member ensemble of the full 3D ocean model is generated. Each member is initialized from a common initial condition with a unique tidal forcing perturbation. The tidal dynamics for the 5 largest constituents, M_2, S_2, N_2, K_1 and O_1, are added to the model dynamics. For each ensemble member, the 41-layer model is run for two months forced by NAVGEM atmospheric fluxes and a tidal forcing perturbation for each constituent. Hourly SSH fields from the last month of each ensemble member are used to calculate the barotropic tidal elevations of the 5 constituents in frequency space, SSH_{T}. The forcing perturbations for the real and imaginary parts of each constituent are generated independently as random fields with scaled maximum magnitudes that differ between constituents, based on the global average of each tidal constituent. For the first 50 members, the forcing perturbation is the convolution of 5000 impulse functions randomly distributed over the ocean and a Gaussian function with a 20° decorrelation length scale. The remaining 50 members are constructed in a slightly different way to increase the ensemble spread. These members have larger amplitude, and are the convolution of 7000 random impulse functions and the same Gaussian functions. An example of a single member of the forcing perturbation ensemble for the M_2 tide is shown in Fig. 2.

4. Simulations and results

The ASEnKF is applied to the ensemble described above. The tidal constituent observations are drawn from the TPXO8-atlas of tidal constituents (Egbert et al., 1994; Egbert and Erofeeva, 2002; with data available at http://volkov.oce.orst.edu/tides/tpxo8atlas.html). The atlas real and imaginary tidal coefficients are interpolated from the 1/30° uniform spherical polar grid to the HYCOM 1/12.5° tripole grid. To reduce the computational size of the matrix inversions in (3), the TPXO8 real and imaginary tidal amplitudes are reduced to a 0.24° grid through a 3 grid-cell by 3 grid-cell boxcar average. The HYCOM tidal solution for each ensemble member are similarly reduced to 0.24° resolution by 3 × 3 boxcar averaging. Before the analysis of the augmented state vector for each constituent, SSH_{T} and ζ, given by (10), can be performed using (3), the observation error ε_k and covariance C_k^{ε} must be chosen. Three different choices will be considered. The first ASEnKF simulation uses a constant white noise observation error of 1 cm everywhere, yielding a solution (the mean of the ensemble analysis) called **T2**. The second simulation, designated **T3**, uses observation errors that vary in space based on tidal amplitude errors from the tables given in Stammer et al. (2014) for TPXO8. In deep water, the observation error for **T3** is 0.5 cm, but increasing to ~16 cm on the continental shelves. The third simulation, **T4**, uses a much smaller constant white noise observation error of 0.5 mm everywhere.

The ASEnKF solutions **T2**, **T3** and **T4** show significant error reduction compared to the earlier simulations **T0** and **T1** almost everywhere in the globe except in the Atlantic basin. This motivated a search for an accurate Atlantic-only solution. In the Atlantic-only solution, the ASEnKF was reduced to include a subset of the global ensemble containing only the SSH_{T} and ζ for the Atlantic. The Atlantic-only solution used a 1 cm observation error and resulted in a marked error estimate reduction in the Atlantic. However, the "Atlantic" ensembles come from the global model, and so the ASEnKF solution and error estimate may not be reliable to the extent that the rest of the global ocean affects tides in the Atlantic. In any case, a new solution, **T5**, is generated by blending the forcing corrections from the Atlantic-only solution with the non-Atlantic forcing corrections from the global solution, **T3**, using a 10° cushion for a smooth transition from one forcing correction to the other. The blending combines the forcing corrections from the Atlantic-only and the global ensembles. It is an *ad hoc* procedure with no theoretical foundation, but it does produce our best overall result when applied to the global model. The M_2 forcing correction for the blended solution **T5** is shown in Fig. 3. The corrections are largest in the Atlantic. In Fig. 4, the M_2 tidal amplitude and phase map from the 3D global model with the forcing correction shown in Fig. 3 and the TPXO8 atlas are shown. On the scale of this figure, the differences between the two maps are

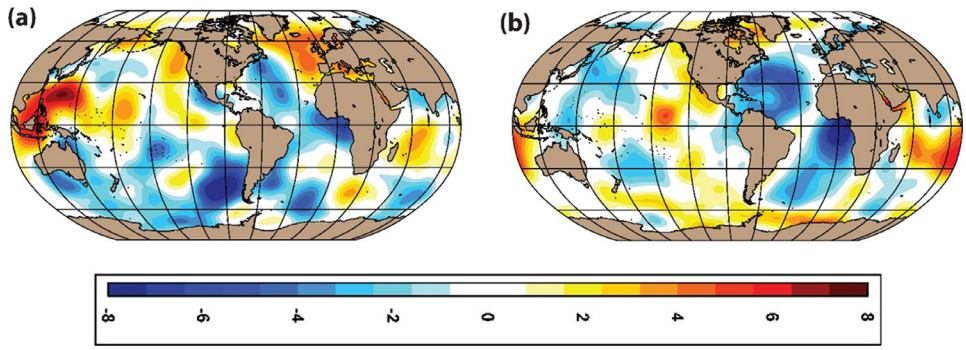

Fig. 2. Sample M2 forcing perturbation fields (cm), real part (a) and imaginary part (b). The forcing perturbation for each part is the convolution of 7000 impulse functions randomly distributed over the ocean and a Gaussian function with a 20° decorrelation length scale and a 10 cm maximum amplitude.

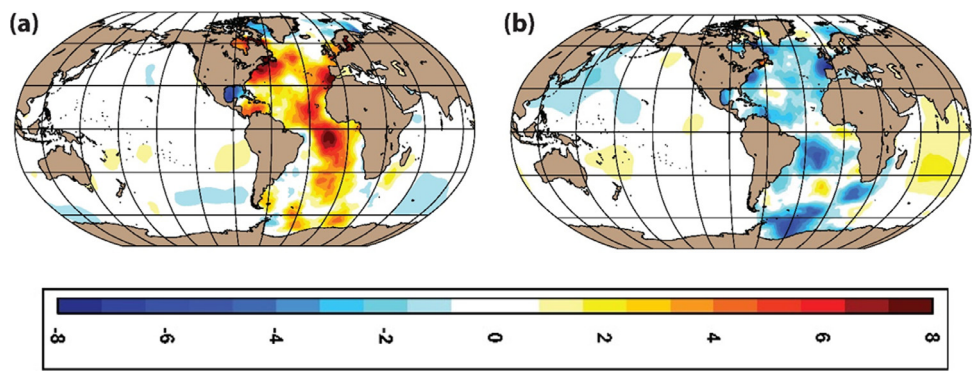

Fig. 3. The real (a) and imaginary part (b) of the tidal forcing correction (cm) obtained by the blended ASEnKF **T5**.

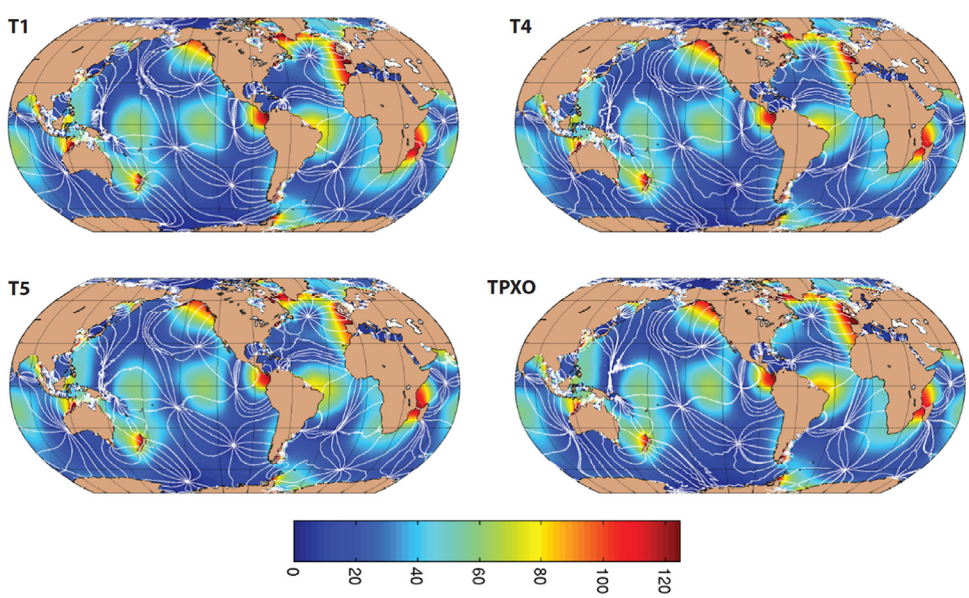

Fig. 4. The M2 barotropic tidal amplitude (cm) and phase (in degrees referenced to Greenwich, with contours drawn every 30 degrees) from **T1**, **T4**, **T5**, and TPXO8 atlas.

not easily seen. In the next section we shall describe the difference between the ASEnKF simulations and TPXO8 in greater detail.

4.1. Tidal elevation errors compared to TPXO8 atlas

To get a quick estimate of the solution performance, the model tide amplitudes from the 3D ocean model with the ASEnKF forcing correction are compared to TPXO8 in space and time, leading to an error time series at each grid point. For brevity, we will focus on the results for M_2 only. Two measures describing the error time series are presented: the RMS error, which is the square root of the time and area-weighted spatial mean of the error variance for all points in the domain for seafloor depths greater than 1000 m, and the median RMS error, which is the spatial median of the square root of the temporal variance at each grid point. The RMS error and median RMS error are listed in Table 1 for the M_2 tidal constituent in both the global (66°S–66°N) and the Atlantic (30°S–66°N) domains. The median RMS error is introduced to avoid possible dominance of outliers. The global RMS error reduces from 7.0 cm for the initial simulation **T0** and 4.4 cm for the intermediate simulation **T1** to 2.6 cm for the blended ASEnKF

Table 1
Global, Atlantic and Global excluding Atlantic M_2 RMS errors and median RMS errors (cm) of the six solutions relative to the TPXO8 Atlas. Errors are computed over gridpoints that are equatorward of 66° and have seafloor depths exceeding 1000 m.

Simulation	Global RMS	Median global RMS	Atlantic RMS	Median Atlantic RMS	Global excluding Atlantic RMS	Median global excluding Atlantic RMS
Initial **T0**	7.0	5.3	6.8	5.6	7.0	4.8
Intermediate **T1**	4.4	3.2	7.3	7.1	3.5	3.5
1 cm constant observation error ASEnKF **T2**	2.8	1.7	5.2	5.2	2.0	1.8
Spatially varying observation error ASEnKF **T3**	3.2	1.6	6.3	6.2	2.0	1.5
0.5 mm constant observation error ASEnKF **T4**	2.8	1.9	4.6	4.6	2.3	1.9
Blended ASEnKF **T5**	2.6	1.7	4.4	3.8	2.1	1.5

solution **T5**. However, there are significant outliers in a few locations with temporal RMS errors far greater than the global mean errors. The peak outliers range from 92 cm for the initial simulation **T0** to 34 cm for the blended ASEnKF solution **T5**. The median global RMS errors are smaller than the global RMS. For the initial solution with its very large outliers, the difference between the global RMS error and the median global RMS error is largest. As mentioned earlier, the errors in the Atlantic are generally greater than the global RMS error. The initial simulation **T0** is an exception with Atlantic errors that are slightly smaller than the intermediate simulation **T1** despite the much smaller global RMS errors for the intermediate simulation. All ASEnKF solutions have smaller global and Atlantic RMS errors compared to the earlier simulations and smaller global RMS errors compared to the Atlantic RMS errors. The numbers in Table 1 show that there is a significant improvement in the accuracy of the M_2 tide from the initial simulation **T0** to intermediate simulation **T1** in the global domain, but degradation in the Atlantic domain. All ASEnKF solutions show further significant improvements in the accuracy of the M_2 tide both in the global and the Atlantic domains. The blended solution **T5** is only slightly improved over the other ASEnKF solutions. Median RMS errors follow similar trends.

Because the TPXO8 atlas tidal amplitudes and phases are used in the ASEnKF, comparison to an independent data set is valuable. In Table 2, the RMS errors relative to 151 deep water gauges are given. TPXO8 has a global RMS error of 0.5 cm relative to these gauges (Stammer et al., 2014). The model simulation errors compared to the gauges are greater than the errors relative to TPXO8 and larger than the errors of TPXO8 relative to the gauges. A reason for the difference may be due to the distribution of the gauges around the globe. More than half the gauges (79) are located in the Atlantic with almost a third of the gauges (47) in the North Atlantic. Ten of the gauges are near the Indonesian Seas. All these gauges are found where all HYCOM simulations have large errors. Similar to Table 1, the ASEnKF solutions **T2–T5** have smaller errors than the initial and intermediate simulations **T0** and **T1**, except in the Atlantic. While the ASEnKF reduces the errors in the simulations, none of the ASEnKF solutions reduces the errors to the levels seen in the TPXO8 atlas, even when the observation errors used in the Kalman filter are extremely small.

4.2. Error histograms

The amplitudes of the tide and the errors relative to TPXO8 are not distributed uniformly over the ocean. Both the largest tides and errors are found in the Atlantic. The differences between the global and Atlantic RMS errors, and between the RMS and the median RMS error, relative to TPXO8, suggest that a limited number of regions with large errors may affect the accuracy estimates. To go beyond the summary table of the RMS and median RMS values, a histogram of the M_2 sea surface height (SSH) spatial RMS errors (computed from the four solutions **T0**, **T1**, **T4** and **T5**) is shown in Fig. 5 for the global, Atlantic and Pacific domains. The histogram provides more detailed information about the distribution of the errors, and a better description of the improvements in the accuracy of the M_2 tide from one simulation to another, than do the global averages in Table 1. It can be seen for example that for the global domain the RMS errors of 2 cm (3 cm) correspond to the 10th (20th), 27th (48th), 53rd (74th) and 59th (78th) percentiles from **T0**, **T1**, **T4** and **T5** respectively. Similarly, the percentiles for the 5 cm RMS errors are 48th, 78th, 90th and 92nd. The RMS errors show that the ASEnKF has produced solutions (**T4** and **T5**) with errors less than or equal to 5 cm in more than 90% of the world's ocean. Corresponding RMS errors for the 90th percentile are 7.5 cm and 12 cm from **T1** and **T0** respectively.

The Atlantic RMS errors, although improved by the assimilation, are still relatively high compared to the global RMS. A good illustration is given by the percentiles for 5 cm RMS errors in the Atlantic domain from the two assimilative solutions **T4** and **T5** (55th and 62nd respectively), compared to 90th and 92nd for the global domain. Note that **T1** is the worst solution in the Atlantic, while T**0** is the worst solution in the global domain. Because the Atlantic domain is included in the computation of the RMS of the global domain, the rest of the world ocean outside of the Atlantic appears to have lower errors than the global domain. For the histograms of the Pacific, the 90 percentile is 3.4 cm and the 50 percentile is 1.5 cm compared to the global 4.4 cm and 2.6 cm, respectively.

4.3. Error maps

The statistics given in Tables 1 and 2 indicate that the errors are largest in the Atlantic. In Fig. 6, maps of the errors relative to TPXO8 for the four simulations, initial with scalar SAL (**T0**), intermediate with iterated SAL, Antarctic shelves and tuned JSL wave drag (**T1**), 0.5 mm constant observation error (**T4**) and blended Atlantic-only and 0.5 mm observation error (**T5**), are shown. In the figure, errors smaller than 2 cm are displayed as white. The improvement in the accuracy of the M_2 tide relative to TPXO8 in **T4** and **T5** occurs nearly everywhere on the globe, as is readily apparent with significant decrease in the warm colors and increase in the white areas. However, significant errors in the Hudson Strait, eastern North Atlantic, and North American coast, equatorial Atlantic, Indonesian Seas and tropical Indian Ocean remain in all solutions. Even in these regions the ASEnKF provides a forcing correction to significantly improve

Table 2
Global, North Atlantic and Global excluding the North Atlantic M_2 RMS errors (in cm) of the six HYCOM solutions and of TPXO8atlas compared to 151 pelagic tide gauges (Stammer et al., 2014).

Simulation	Global RMS 151 gauges	North Atlantic RMS 47 gauges	Global excluding North Atlantic RMS 104 gauges
Initial **T0**	7.8	7.7	7.8
Intermediate **T1**	6.8	10.9	3.5
1 cm constant observation error ASEnKF **T2**	5.2	8.7	2.2
Spatially varying observation error ASEnKF **T3**	5.9	10.0	2.0
0.5 mm constant observation error ASEnKF **T4**	4.7	7.6	2.5
Blended ASEnKF **T5**	4.6	7.7	2.0
TPXO8atlas	0.5	0.6	0.5

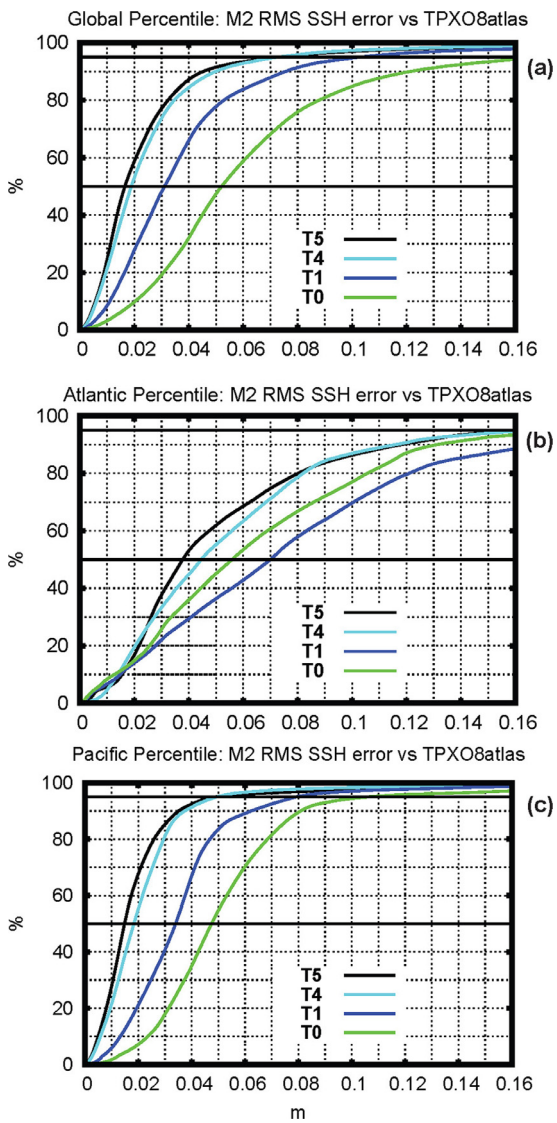

Fig. 5. Histograms of M_2 SSH RMS error relative to TPXO8 for the global (a), the Atlantic (b) and the Pacific (c) domains from the initial simulation **T0** (green), intermediate simulation **T1** (blue), 0.5 mm constant observation error ASEnKF **T4** (cyan) and blended ASEnKF **T5** (black). (For interpretation of the references to color in this figure legend, the reader is referred to the web version of this article.)

3D ocean model tidal amplitudes and phases, but large errors still exist.

5. Discussion

The ASEnKF leads to significant reduction in the global RMS error of the M_2 tide compared to the non-assimilative initial simulation with a scalar SAL and the non-assimilative intermediate simulation with iterated SAL, Antarctic shelves and tuned JSL wave drag. However, none of the ASEnKF solutions can reduce the errors to the level of the observation errors used in the analysis. The analysis cannot reduce the error if the background error covariance is much greater than the observation error or if the ensemble generating the background error covariance does not include the spatial variability of the true model error. The background error covariance is the mean of the variance across the ensemble and only describes structures found in the members of the ensemble. In the analysis, the term $(\mathbf{HBH}^{\mathrm{T}} + \mathbf{C}_{\varepsilon})^{-1}$ $(\mathbf{Y}\text{-}\mathbf{HZ})$ is not calculated directly. Rather, we use a singular value decomposition to factor the symmetric positive definite matrix $(\mathbf{HBH}^{\mathrm{T}} + \mathbf{C}_{\varepsilon})$ as $\mathbf{UDU}^{\mathrm{T}}$ where $\mathbf{U}$ is an orthogonal matrix whose columns are the eigenvectors of $(\mathbf{HBH}^{\mathrm{T}} + \mathbf{C}_{\varepsilon})$ and $\mathbf{D}$ is a diagonal matrix whose nonzero elements are the eigenvalues. As pointed out by Richman et al. (2005), the analysis increments are assembled from the projection of the errors between the observed tide and the ensemble member tides onto the eigenvectors of the background error covariance. Thus, if the forcing perturbations do not generate a sea level elevation that resembles the error, then no correction to reduce this error can be made with the ASEnKF.

The perturbations used in the ASEnKF, similar to the example shown in Fig. 2, are assembled from random in space instances of large scale Gaussians. The length scales of these perturbations are similar to the length scales of the errors found in the initial simulation **T0** and intermediate simulation **T1**. The actual errors for the ASEnKF solutions have different length scales, which are not represented well by the forcing perturbations.

As shown by many authors (e.g., Wunsch, 1972; Garrett and Greenberg, 1977; Heath, 1981; Platzman et al., 1981; Müller, 2007), the global tidal system is weakly resonant, especially in the North Atlantic. Recently it has been shown that the tides in coastal areas are not just passive receptors of the global ocean tides, but actually have a large "back-effect" upon the open-ocean tides (Arbic et al., 2007, 2009; Arbic and Garrett, 2010). The latter three studies showed that changes in the geometry of a region having large resonant coastal tides (e.g., Hudson Strait, the Bay of Fundy, and the English Channel) can impact the tide field throughout the globe. All of this suggests that the perturbation fields in coastal areas will impact the global tide problem significantly. Thus, the perturbation fields for our ASEnKF should be representative of coastal tidal conditions in coastal regions, meaning that in such regions the perturbations should have smaller horizontal scales and larger amplitudes. However, for the sake of simplicity, the perturbations utilized in this first study of the ASEnKF in HYCOM tides simulations do not differentiate between coastal and open-ocean gridpoints.

The errors after applying the ASEnKF correction fields are largest in the Atlantic, near the Indonesian Seas and in the Indian Ocean. Since the Atlantic is relatively isolated from the other ocean basins, an Atlantic-only correction was obtained by cutting out the Atlantic from the Global ensemble. This Atlantic-only correction gave the best ASEnKF estimate of its error for the Atlantic, and it was blended with our best correction for the rest of the globe. The global tidal solution

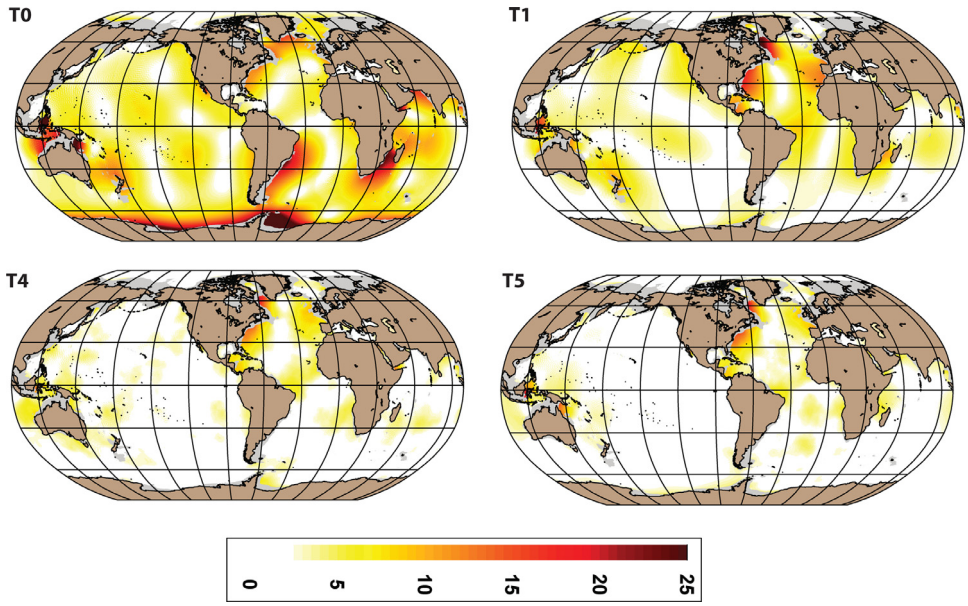

Fig. 6. Maps of the M_2 RMS error (cm) between the HYCOM simulations and TPXO8: **T0**, initial 8 constituent simulation with scalar SAL and Garner (2005) wave drag; **T1**, intermediate 5 constituent simulation with bathymetry extended to include floating Antarctic ice shelves, tuned Jayne and St. Laurent (2001) wave drag, and iterated SAL; **T4**, ASEnKF predicted tide using a 0.5 mm constant global observation error; **T5**, Blended ASEnKF predicted tide combining an Atlantic-only prediction with 1 cm observation error and **T3** for the rest of the ocean.

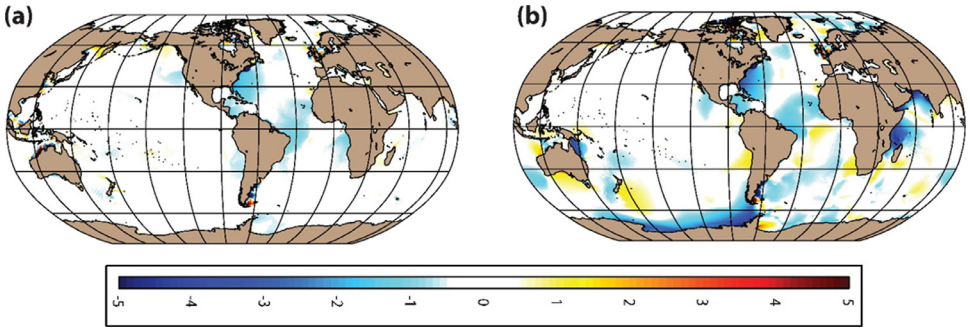

Fig. 7. The difference (cm) of the RMS errors between the M_2 tide predicted by the ASEnKF analysis and TPXO8 and the M_2 tide obtained in the full 3D global ocean model and TPXO8 for (a) **T4** and (b) **T5**. In regions with blue colors, the tides in the 3D ocean model have larger errors relative to TPXO8 than the ASEnKF predicted tide, while warmer colors represent regions where the 3D ocean model tide is closer to TPXO8 than the ASEnKF predicted tide. (For interpretation of the references to color in this figure legend, the reader is referred to the web version of this article.)

obtained from this ad-hock correction field, **T5**, has slightly smaller errors than **T4**, but its errors are still larger than the observation errors in the analysis. Thus, the large scale forcing perturbations generating the ensemble are unable to adequately model the tides in the Atlantic.

The ASEnKF analysis provides a prediction of the tide as well as the optimal forcing correction for the 3D ocean model. The predicted tide from the ASEnKF is not the same as the tide predicted by a simulation of the full 3D ocean model, which contains mesoscale eddies and the general circulation, using the optimal forcing correction. In Fig. 7, the difference between the errors of the ASEnKF predicted tide for two cases (**T4** with extremely small observation error and **T5** the blended solution) and TPXO8, and the errors of the 3D model tides generated by the forcing correction for the two cases and TPXO8, are shown. In the figure, areas with negative difference (cold colors) have larger errors relative to TPXO8 in the 3D model with the forcing correction compared to the errors of the ASEnKF predicted tide relative to TPXO8. For **T4** with a constant extremely small observation error, the differences are small and, when they differ, the 3D model tides tend to be less accurate. For this case, except in the Atlantic, the predicted tide from the state estimation is very close to the 3D ocean model tide with the optimal forcing correction. The differences between the errors of the predicted and modeled tides are smaller than the errors of either solution and TPXO8. This result indicates that the ASEnKF is correctly capturing the behavior of the model, except perhaps in the Atlantic. For **T5**, the differences in the errors between the predicted and modeled tides are larger, which indicates that the Atlantic-only analysis and the blending with the global analysis is not entirely successful, even though it produces the smallest errors relative to TPXO8 overall. Visual inspection of Fig. 6 shows that the blended ASEnKF solution **T5** has larger errors in the Southern Ocean and near Australia and Indonesia than the extremely small observation error ASEnKF solution **T4**. These are the same regions with large errors between the 3D ocean model tide and TPXO8 compared to the predicted tide and TPXO are found in Fig. 7. We expect that deficiencies with the ensemble generated by the large spatial scale perturbations and the corresponding background error covariance used in the analysis are sources of these discrepancies. The forcing correction generated by an ensemble of large spatial scale perturbations cannot correct for the model deficiencies on small spatial scales.

6. Conclusions

The ASEnKF approach, which provides corrections to the model forcing to reduce the HYCOM tide errors, shows promise. All ASEnKF solutions had smaller errors than the intermediate simulation **T1**

with iterated SAL, Antarctic shelves and a tuned JSL wave drag. However, none of the ASEnKF solutions could describe the small-scale and resonant behavior of the tides in the Atlantic and near the Indonesian Seas. This may be due to the fact that the perturbations used to generate the ensemble for the ASEnKF had large scales.

Acknowledgments

We thank Richard Ray for providing the 151 tide gauge data used in Table 2. HEN and IS were supported by the projects, "NCOM-4DVAR", "A multiscale Approach for Assessing Predictability of ASW environment", and "Extending Predictability in Coastal Environments", sponsored by Office of Naval Research (ONR). JGR, JFS and AJW were supported by the projects "HYCOM global ocean forecast skill assessment", sponsored by ONR and the National Ocean Partnership Program (NOPP) sponsored "Improving Global Surface and Internal Tides through Two-Way Coupling with High Resolution Coastal Models." BKA gratefully acknowledges support from (ONR) grants N00014-11-1-0487 and N00014-15-1-2288. The model results were obtained on a Cray XC30 at the Navy DoD Supercomputing Resource Center under the FY13-15 Department of Defense HPC Challenge Project "Global Earth System Prediction". This is NRL contribution NRL/JA/7320-15-2596. The authors are grateful to the anonymous reviewers; their comments helped to improve the quality of this paper.

References

Accad, Y., Pekeris, C.L., 1978. Solution of tidal equations for M2 and S2 tides in world oceans from a knowledge of tidal potential alone. Philos. Trans. R. Soc. A290, 235–266.

Ansong, J.K., Arbic, B.K., Buijsman, M.C., Richman, J.G., Shriver, J.F., Wallcraft, A.J., 2015. Indirect evidence for substantial damping of low-mode internal tides in the open ocean. J. Geophys. Res. Oceans 120, 6057–6071.

Arbic, B.K., Garner, S.T., Hallberg, R.W., Simmons, H.L., 2004. The accuracy of surface elevations in forward global barotropic and baroclinic tide models. Deep-Sea Res. II 51, 3069–3101.

Arbic, B.K., Karsten, R.H., Garrett, C., 2009. On tidal resonance in the global ocean and the back-effect of coastal tides upon open-ocean tides. Atmosphere-Ocean 47, 239–266. doi:10.3137/OC311.2009.

Arbic, B.K., St-Laurent, P., Sutherland, G., Garrett, C., 2007. On the resonance and influence of tides in Ungava Bay and Hudson Strait. Geophys. Res. Lett 34, L17606. doi:10.1029/2007GL030845.

Arbic, B.K., Garrett, C., 2010. A coupled oscillator model of shelf and ocean tides. Cont. Shelf Res. 30, 564–574. doi:10.1016:/j.csr.2009.07.008.

Arbic, B.K., Wallcraft, A.J., Metzger, E.J., 2010. Concurrent simulation of the eddying general circulation and tides in a global ocean model. Ocean Model. 32, 175–187. doi:10.1016/j.ocemod.2010.01.007.

Arbic, B.K, Richman, J.G., Shriver, J.F., Timko, P.G., Metzger, E.J., Wallcraft, A.J., 2012. Global modeling of internal tides within an eddying ocean general circulation model. Oceanography 25, 20–29. doi:10.5670/oceanog.2012.38.

Baek, S.-J., Hunt, B.R., Kalnay, E., Ott, E., Szunyogh, I., 2006. Local ensemble Kalman filtering in the presence of model bias. Tellus 58A, 293–306.

Bennett, A.F., 2002. Inverse Modeling of the Ocean and Atmosphere. Cambridge University Press, p. 234.

Buijsman, M.C., Arbic, B.K., Green, J.A.M., Helber, R.W., Richman, J.G., Shriver, J.F., Timko, P.G., Wallcraft, A.J., 2015. Optimizing internal wave drag in a forward barotropic model with semidiurnal tides. Ocean Model. 85, 42–55.

Chassignet, E.P., Hurlburt, H.E., Smedstad, O.M., Halliwell, G.R., Wallcraft, A.J., Metzger, E.J., Blanton, B.O., Lozano, C., Rao, D.B., Hogan, P.J., Srinivasan, A., 2009. Generalized vertical coordinates for eddy-resolving global and coastal ocean forecasts. Oceanography 19 (1), 20–31.

Egbert, G.D., Bennett, A.F., Foreman, M.G.G., 1994. TOPEX/POSEIDON tides estimated using a global inverse model. J. Geophys. Res. 99 (C12), 24821–24852. doi:10.1029/94JC01894.

Egbert, G.D., Erofeeva, S.Y., 2002. Efficient inverse modeling of barotropic ocean tides. J. Atmos. Ocean. Tech. 19, 183–204.

Egbert, G.D., Ray, R.D., 2001. Estimates of M2 tidal energy dissipation from TOPEX/Poseidon altimeter data. J. Geophys. Res. 106 (C10) 22,475-22,502.

Egbert, G.D., Ray, R.D., Bills, B.G., 2004. Numerical modeling of the global semidiurnal tide in the present day and in the Last Glacial Maximum. J. Geophys. Res. 109, C03003. doi:10.1029/2003JC001973.

Evensen, G., 1994. Sequential data assimilation with a nonlinear quasi-geostrophic model using Monte-Carlo methods to forecast error statistics. J. Geophys. Res. 99, 10143–10162.

Fertig, E.J., Baek, S.-J., Hunt, B.R., Ott, E., Szunyogh, I., Aravéquia, J.A., Kalnay, E., Li, H., Liu, J., 2009. Observation bias correction with an ensemble Kalman filter. Tellus 61A, 210–226.

Garner, S.T., 2005. A topographic drag closure built on an analytical base flux. J. Atmos. Sci. 62, 2302–2315.

Garrett, C., 2003. Internal tides and ocean mixing. Science 301 (5641), 1858–1859. doi:10.1126/science.1090002.

Garrett, C.J.R., Munk, W.H., 1975. Space-timescales of internal waves. A progress report.. J. Geophys. Res 80, 291–297.

Garrett, C., Greenberg, D., 1977. Predicting changes in tidal regime: the open boundary problem. J. Phys. Oceanogr. 7, 171–181.

Gelb, A., 1974. Applied Optimal Estimation. The MIT Press, p. 374.

Gordeev, R.G., Kagan, B.A., Polyakov, E.V., 1977. The effects of loading and self-attraction on global ocean tides: the model and the results of a numerical experiment. J. Phys. Oceanogr. 7, 161–170.

Heath, R.A., 1981. Estimates of the resonant period and Q in the semi-diurnal tidal band in the North Atlantic and Pacific Oceans. Deep-Sea Res. Part A 28, 481–493.

Hendershott, M.C., 1972. The effects of solid earth deformation on global ocean tides. Geophys. J. R. Astron. Soc. 29, 389–402.

Hogan, T.F., Liu, M., Ridout, J.A., Peng, M.S., Whitcomb, T.R., Ruston, B.C., Reynolds, C.A., Eckermann, S.D., Moskaitis, J.R., Baker, N.L., McCormack, J.P., Viner, K.C., McLay, J.G., Flatau, M.K., Xu, L., Chen, C., Chang, S.W., 2014. The navy global environmental model. Oceanography 27 (3), 116–125. doi:10.5670/oceanog.2014.73, http://dx.doi.org/ .

Holloway, P.E., 1996. A numerical model of internal tides with application to the Australian North West Shelf. J. Phys. Oceanogr. 26, 21–37.

Jayne, S.R., St. Laurent, L.C., 2001. Parameterizing tidal dissipation over rough topography. Geophys. Res. Lett. 28, 811–814. doi:10.1029/2000GL012044.

Jazwinski, A.H., 1970. Stochastic Processes and Filtering Theory. Academic Press, p. 376.

Kelly, S.M., Nash, J.D., 2010. Internal-tide generation and destruction by shoaling internal tides. Geophys. Res. Lett 37, L23611. doi:10.1029/2010GL045598.

Kerry, C.G., Powell, B.S., Carter, G.S., 2013. Effects of remote generation sites on model estimates of M2 internal tides in the Philippine Sea. J. Phys. Oceanogr. 43, 187–204.

Lyard, F.H., Lefevre, F., Letellier, T., Francis, O., 2006. Modelling the global ocean tides: modern insights from FES2004. Ocean Dyn. 56, 394–415. doi:10.1007/s10236-006-0086-x.

Merrifield, M.A., Holloway, P.E., Shaun Johnston, T.M., 2001. The generation of internal tides at the Hawaiian ridge. Geophys. Res. Lett. 28 (4), 559–562.

Metzger, E.J., Smedstad, O.M., Thoppil, P.G., Hurlburt, H.E., Cummings, J.A., Wallcraft, A.J., Zamudio, L., Franklin, D.S., Posey, P.G., Phelps, M.W., Hogan, P.J., Bub, F.L., Dehaan, C.J., 2014. US Navy operational global ocean and Arctic ice prediction systems. Oceanography 27 (2), 10–21.

Müller, M., Cherniawsky, J.Y., Foreman, M.G.G., von Storch, J.-S., 2012. Global map of M_2 internal tide and its seasonal variability from high resolution ocean circulation and tide modeling. Geophys. Res. Lett. 39, L19607. doi:10.1029/2012GL053320.

Müller, M., Arbic, B.K., Richman, J.G., Shriver, J.F., Kunze, E.L., Scott, R.B., Wallcraft, A.J., Zamudio, L., 2015. Toward an internal gravity wave spectrum in global ocean models. Geophys. Res. Lett. 42, 3474–3481.

Müller, M., 2007. The free oscillations of the world ocean in the period range 8 to 165 hours including the full loading effect. Geophys. Res. Lett 34, L05606. doi:10.1029/2006GL028870.

Munk, W., Wunsch, C., 1998. Abyssal recipes II: energetics of tidal and wind mixing. Deep-Sea Res. II 45, 1977–2010.

Ngodock, H., Carrier, M., 2014. A 4DVAR system for the navy coastal ocean model. Part II: strong and weak constraint assimilation experiments with real observations in monterey bay. Mon. Weather Rev. 142, 2108–2117.

Platzman, G.W., Curtis, G.A., Hansen, K.S., Slater, R.D., 1981. Normal modes of the World Ocean. Part II: description of modes in the period range 8 to 80 hours. J. Phys. Oceanogr. 11, 579–603.

Ponte, A.L., Cornuelle, B.D., 2013. Coastal numerical modelling of tides: sensitivity to domain size and remotely generated internal tide. Ocean Model. 62, 17–26.

Ray, R.D., 1998. Ocean self-attraction and loading in numerical tidal models. Mar. Geodesy 21, 181–192.

Ray, R.D., Byrne, D.A., 2010. Bottom pressure tides along a line in the southeast Atlantic Ocean and comparisons with satellite altimetry. Ocean Dyn. 60, 1167–1176.

Ray, R.D., Mitchum, G.T., 1996. Surface manifestation of internal tides generated near Hawaii. Geophys. Res. Lett. 23, 2101–2104.

Reichle, R.H, McLaughlin, D.B., Entekhabi, D., 2002. Hydrologic data assimilation with the ensemble Kalman filter. Mon. Weather Rev. 130, 103–114.

Richman, J.G., Arbic, B.K., Shriver, J.F., Metzger, E.J., Wallcraft, A.J., 2012. Inferring dynamics from the wavenumber spectra of an eddying global ocean model with embedded tides. J. Geophys. Res. 117, C12012. doi:10.1029/2012JC008364.

Richman, J.G., Miller, R.N., Spitz, Y.H., 2005. Error estimates for assimilation of satellite sea surface temperature data in ocean climate models. Geophys. Res. Lett. 32, L18608. doi:10.1029/2005GL023591.

Rosmond, T.E., Teixeira, J., Peng, M., Hogan, T.F., Pauley, R., 2002. Navy operational global atmospheric prediction system (NOGAPS): forcing for ocean models. Oceanography 15, 99–108.

Shriver, J.F., Arbic, B.K., Richman, J.G., Ray, R.D., Metzger, E.J., Wallcraft, A.J., Timko, P.G., 2012. An evaluation of the barotropic and internal tides in a high resolution global ocean circulation model. J. Geophys. Res. 117, C10024. doi:10.1029/2012JC008170.

Shriver, J.F., Richman, J.G., Arbic, B.K., 2014. How stationary are the internal tides in a high-resolution global ocean circulation model? J. Geophys. Res. Oceans 119, 2769–2787. doi:10.1002/2013JC009423.

Stammer, D., Ray, R.D., Andersen, O.B., Arbic, B.K., Bosch, W., Carrère, L., Cheng, Y., Chinn, D.S., Dushaw, B.D., Egbert, G.D., Erofeeva, S.Y., Fok, H.S., Green, J.A.M., Griffiths, S., King, M.A., Lapin, V., Lemoine, F.G., Luthcke, S.B., Lyard, F., Morison, J., Müller, M., Padman, L., Richman, J.G., Shriver, J.F., Shum, C.K., Taguchi, E., Yi, Y., 2014. Accuracy assessment of global barotropic ocean tide models. Rev. Geophys. 52, 243–282. doi:10.1002/2014RG000450.

Stepanov, V.N., Hughes, C.W., 2004. Parameterization of ocean self-attraction and loading in numerical models of the ocean circulation. J. Geophys. Res. 109, C03037. doi:10.1029/2003JC002034.

Taguchi, E., Stammer, D., Zahel, W., 2014. Inferring deep ocean tidal energy dissipation from the global high-resolution data-assimilative HAMTIDE model. J. Geophys. Res. 119, 4573–4592. doi:10.1002/2013JC009766.

Timko, P.G., Arbic, B.K., Richman, J.G., Scott, R.B., Metzger, E.J., Wallcraft, A.J., 2012. Skill tests of three-dimensional tidal currents in a global ocean model: a look at the North Atlantic. J. Geophys. Res. 117, C08014. doi:10.1029/2011JC007617.

Timko, P.G., Arbic, B.K., Richman, J.G., Scott, R.B., Metzger, E.J., Wallcraft, A.J., 2013. Skill testing a three-dimensional global tide model to historical current meter records. J. Geophys. Res. Oceans 118, 6914–6933. doi:10.1002/2013JC009071.

Waterhouse, A.F., MacKinnon, J.A., Nash, J.D., Alford, M.H., Kunze, E., Simmons, H.L., Polzin, K.L., St. Laurent, L.C., Sun, O.M., Pinkel, R., Talley, L.D., Whalen, C.B., Huussen, T.N., Carter, G.S., Fer, I., Waterman, S., Naveira Garabato, A.C., Sanford, T.B., Lee, C.M., 2014. Global patterns of diapycnal mixing from measurements of the turbulent dissipation rate. J. Phys. Oceanogr 44 (7), 1854–1872. doi:10.1175/JPO-D-13-0104.1.

Weaver, A., Courtier, P., 2001. Correlation modeling on the sphere using a generalized diffusion equation. Q. J. R. Meteorol. Soc. 127, 1815–1846.

Wunsch, C., 1972. Bermuda sea level in relation to tides, weather, and baroclinic fluctuations. Rev. Geophys. 10, 1–49.

Zupanski, D., Zupanski, M., 2006. Model error estimation employing an ensemble data assimilation approach. Mon. Weather Rev. 134, 1337–1354.